Oral presentation | Multi-phase flow

Multi-phase flow-III

Mon. Jul 15, 2024 4:30 PM - 6:30 PM Room D

[3-D-01] A Smoothed-Terrain-Following Coordinate System for Modeling Gravity-Driven Flows in Depth-Averaged Approach

*Yih-Chin Tai[1], Hock-Kiet Wong[1], Ching-Yuan Ma[1] （1. Dept. Hydraulic and Ocean Engineering, National Cheng Kung University, Tainan, Taiwan）

Keywords: gravity-driven flows, depth-averaged approach, terrain-following coordinate, two-phase debris flows

Twelfth International Conference on
Computational Fluid Dynamics (ICCFD12),
Kobe, Japan, July 14-19, 2024

ICCFD12-2024-xxxx

A Smoothed-Terrain-Following Coordinate System for Modeling Gravity-Driven Flows in Depth-Averaged Approach

Y.C. Tai, H.K. Wong and C.Y. Ma
Corresponding author: yctai@ncku.edu.tw
Dept. Hydraulic and Ocean Engineering, National Chung Kung University, Taiwan

1 Introduction

The present study demonstrates a strategy for formulating the model equations for sediment-related gravity-driven mass flows moving in rugged mountainous areas. Given that these hazardous flows are typically thin compared to their lateral extension, and considering the extensive computational domain, numerical simulations often rely on models with depth-integrated governing equations to achieve high computational efficiency. Therefore, the choice of coordinate system becomes crucial for providing an appropriate description. Many models for simulating these hazardous flows are presented in Cartesian coordinates due to the ease of mathematical formulation and the associate numerical implementation. However, there are several intrinsic shortcomings when simulating these hazardous flows using depth-averaged model equations given in Cartesian coordinates, e.g., (cf. Fig. 1)

- Ambiguous definition of flow thickness: counted in vertical or normal direction?
- Deviated velocity direction for deep slopes;
- Once the erosion/deposition rate is velocity-dependent, the direction deviation would induce incorrect rate.

As shown in Fig. 1b, for a uniform flow in an inclined channel, the flow depth (h_{Cart}) defined in the vertical-horizontal-oriented Cartesian coordinates O_{xy} differs from the one (h_{TH}) defined in the terrain-following coordinates $O_{\xi\zeta}$. Despite the difference in depth definition, the volume of a flow with length L remains unchanged. However, the gravity-driven acceleration reads $a_x = g\tan\theta$ (with g as the gravitational acceleration) in O_{xy}, while it is $a_\xi = g\sin\theta$ in $O_{\xi\zeta}$. Consequently, the projection of a_ξ onto the horizontal x-axis is $a_{\xi,x} = g\sin\theta\cos\theta$. Hence, we have $a_{\xi,x} = a_x(\cos\theta)^2$, indicating that a higher acceleration exists in Cartesian coordinates at deep slopes. The discrepancy becomes significant when the slope is deep (e.g., with respect to a slope of $1/3.735 = \tan 15°$, the discrepancy would be approximately 7.2%.). So, when using the Cartesian coordinate system, a gradual variation in topography should be a prerequisite condition for more accurate computation.

On the other hand, the terrain-fitted coordinate system [1, 2, 3] may address these shortcomings, but its applicability is limited by the shallow curvature of the topography. As suggested in [4], we propose a smoothed-terrain-following coordinate system in which the coordinates are adjusted to follow

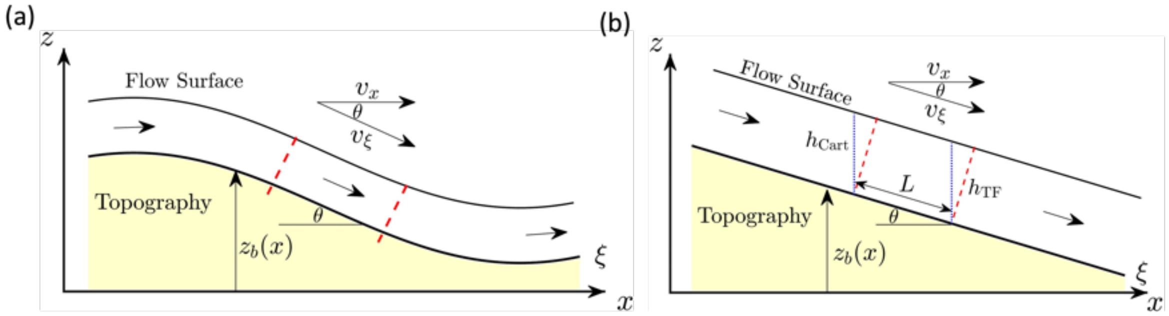

Figure 1: (a) Coordinate system O_{xz} and $O_{\xi\zeta}$, where significant deviation for the velocity direction can be found at deep slopes. (b) A uniform flow along a inclined channel infinitely long.

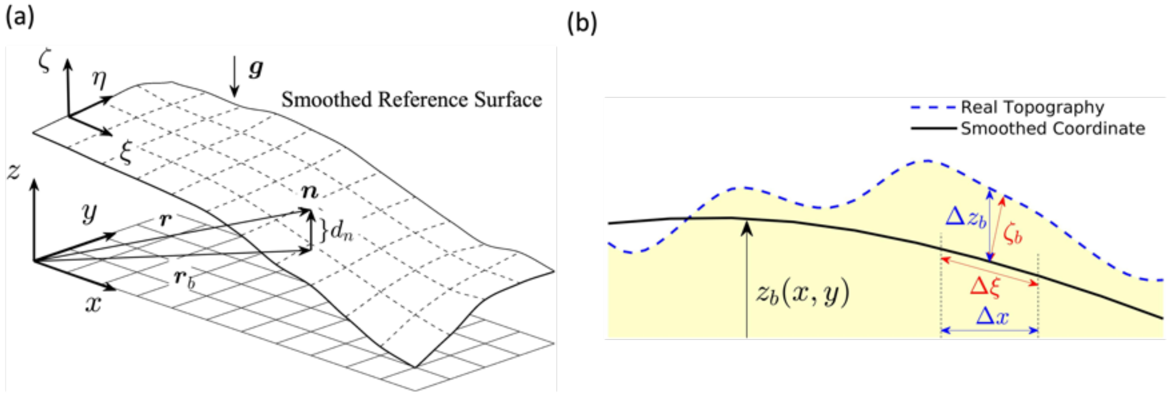

Figure 2: (a) Coordinate systems O_{xyz} and $O_{\xi\eta\zeta}$, where the position vector of a point above the smoothed-reference topographic surface is denoted by its distance and the associated projection on the surface, $\boldsymbol{r} = \boldsymbol{r}_b + d_n\,\boldsymbol{n}$. (b) The sub-topography, $\zeta_{\rm b}$, is added on the smoothed (coordinate) surface to account for the variation of the local topography.

the smoothed basal surface. A "sub-topography" is placed on the smoothed surface to replicate the high-resolution elevation provided in the digital elevation map (DEM) or when erosion/deposition occurs. In addition to the presentation of the model equations, various numerical examples will be illustrated to demonstrate the superior key features of the present proposal. The CUDA-GPU techniques are employed in the numerical implementation (coding) for a high-performance computation, and a 3D user-interactive illustration platform (ANSI-Platform) has been developed for scenario investigation as an efficient powerful tool for hazard assessment, risk analysis, or evaluating the planned disaster mitigation countermeasures.

2 Model equations in a smoothed-terrain-following coordinate system

2.1 Smoothed-terrain-following coordinate system

In the modern Geographic Information System (GIS) system, the topography is represented by the digital elevation model (DEM), which is a set of altitudes of terrain locations over a horizontal regular grid. The DEM therefore fits a vertical-horizontal-oriented Cartesian coordinates O_{xyz}, where the x- and y-axis coincide with horizontal grids and the z-direction points upwards for the elevation.

Assuming the DEM-defined topography to be a smooth surface, a terrain-fitted coordinate system $O_{\xi\eta\zeta}$ can be introduced [1, 2], where the projections of ξ-axis and η-axis on the horizontal plane coincide with x-axis and y-axis, respectively (see Fig. 2a). Letting $\boldsymbol{\Omega}_{\rm b}$ be the transformation matrix for points at the topographic surface, and $\boldsymbol{\tau}_\xi$, $\boldsymbol{\tau}_\eta$ and $\boldsymbol{\tau}_\zeta$, denote the corresponding basis vectors, the unit normal vector can be determined by

$$\boldsymbol{n} = \boldsymbol{g}_\zeta = \frac{\boldsymbol{\tau}_\xi \times \boldsymbol{\tau}_\eta}{||\boldsymbol{\tau}_\xi \times \boldsymbol{\tau}_\eta||} = n_x \hat{\boldsymbol{e}}_x + n_y \hat{\boldsymbol{e}}_y + n_z \hat{\boldsymbol{e}}_z\,, \tag{1}$$

where $\hat{\boldsymbol{e}}_x$, $\hat{\boldsymbol{e}}_y$ and $\hat{\boldsymbol{e}}_z$ are the basis vectors of O_{xyz}. For a point above the topographic surface with a distance d_n, its position vector $\boldsymbol{r}$ can be decomposed by the projection vector of the point on the topographic surface $\boldsymbol{r}_b$ and the distance d_n to the basal surface, i.e.,

$$\boldsymbol{r} = \boldsymbol{r}_b + d_n\,\boldsymbol{n}\,, \tag{2}$$

see Fig. 2a. The expression (2) is not applicable always. The point is uniquely defined by (2), only when the distance d_n is less than the local curvature radius.

Despite adopting the assumption of shallow flow, the flow thickness may exceed the local curvature radius, thereby violating the unique description of (2). As a compromise, we propose to define the terrain-following coordinates on a smoothed reference surface with respect to a highly rugged topography. That is, the topographic elevation can be smoothed by some smoothing filter, e.g., the 3×3 or 5×5 Gaussian filter, with which the smoothing process can be performed for several times to meet the shallow curvature requirement. Following [4], we applied the 3 × 3 smoothing filter,

$$\begin{aligned} z^{\text{smoothed}}_{b,(i,j)} = \;& 0.0751\, z^b_{i-1,j+1} + 0.1238\, z^b_{i,j+1} + 0.0751\, z^b_{i+1,j+1} \;+ \\ & 0.1238\, z^b_{i-1,j} + 0.2044\, z^b_{i,j.} + 0.1238\, z^b_{i+1,j} \;+ \\ & 0.0751\, z^b_{i-1,j-1} + 0.1238\, z^b_{i,j-1} + 0.0751\, z^b_{i+1,j-1}\,, \end{aligned} \tag{3}$$

for data point (i, j) to construct the smoothed reference surface for the terrain-following coordinates. With this smoothing approach, a "sub-topography", ζ_b, is introduced to overlay the smoothed topographic surface and replicate the topography defined by the DEM, see Fig. 2b. It should be noted that the sub-topography ζ_b is accounted for along the normal direction defined on the smoothed reference basal surface. Meanwhile, $\triangle z_b$, denoting the elevation difference in the smoothing process, is calculated vertically. Hence, ζ_b is determined by the elevation difference $\triangle z_b$ and the mesh sizes ($\triangle x$ and $\triangle \xi$) in the two coordinate systems,

$$\zeta_b = \triangle z_b \, \triangle x / \triangle \xi \,, \tag{4}$$

for ensuring the mass conservation within the mesh $\triangle x$, cf. Fig. 2b. It is noted that the magnitude of ζ_b varies when erosion or deposition takes place.

2.2 Two-phase model over erodible surface for debris flows

In the present study, we employ a two-phase model over erodible surface proposed by Wong et al., [5] to investigate the proposed approach of smoothed-terrain-following coordinate. The flow body and the ground are supposed to be composed by two constituents, the grain particles and the viscous interstitial fluid. The local basal surface (sub-topography over the smoothed basal reference surface) evolves in accordance with the local erosion (volume) rate as

$$\frac{\partial \zeta_{\text{b}}}{\partial t} = \frac{\mathcal{E}^{\text{s}}}{\phi^{\text{s}}_{\text{b}}} = \frac{\mathcal{E}^{\text{f}}}{\phi^{\text{f}}_{\text{b}}} \,. \tag{5}$$

In (5), $\mathcal{E}^{\text{s}}$ and $\mathcal{E}^{\text{f}}$ represent the erosion (volume) rates for the solid and fluid phase, respectively, and $\phi^{\text{s,f}}_{\text{b}}$ with $\phi^{\text{s}}_{\text{b}} + \phi^{\text{f}}_{\text{b}} = 1$ denote the porosities of the erodible bed. Here, $\phi^{\text{s}}_{\text{b}} + \phi^{\text{f}}_{\text{b}} = 1$ means that the entrained or deposited material is fully saturated during the process.

The model equations are identical to the ones in Wong et al., [5] and given in dimensionless form, where a characteristic length $\mathcal{L}$ of the flow body along the smoothed reference basal surface is introduced with a respective characteristic flow thickness $\mathcal{H}$. In deriving the resultant model equations, a small aspect ratio $\epsilon = \mathcal{H}/\mathcal{L} \ll 1$ is utilized to isolate the physically insignificant terms. The resultant mass balance equations for the solid and fluid phases read

$$\frac{\partial}{\partial t}(J_{\text{b}} h^{\text{s}}) + \frac{\partial}{\partial \xi}(J_{\text{b}} h^{\text{s}} v^{\text{s}}_{\xi}) + \frac{\partial}{\partial \eta}(J_{\text{b}} h^{\text{s}} v^{\text{s}}_{\eta}) = \epsilon J_{\text{b}} \mathcal{E}^{\text{s}} \tag{6}$$

and

$$\frac{\partial}{\partial t}(J_{\text{b}} h^{\text{f}}) + \frac{\partial}{\partial \xi}(J_{\text{b}} h^{\text{f}} v^{\text{f}}_{\xi}) + \frac{\partial}{\partial \eta}(J_{\text{b}} h^{\text{f}} v^{\text{f}}_{\eta}) = \epsilon J_{\text{b}} \mathcal{E}^{\text{f}} \,, \tag{7}$$

respectively, where $J_{\text{b}} = \det(\boldsymbol{\Omega}_{\text{b}})$, $h^{\text{s}} = h\phi^{\text{s}}$ and $h^{\text{f}} = h\phi^{\text{f}}$ with h representing the total flow thickness, $(\phi^{\text{s}}, \phi^{\text{f}})$ and (v_{ξ}, v_{η}) denote the depth-averaged volume concentrations and the tangential components of the depth-averaged velocity in the terrain-following coordinate system, respectively.

As given in [5], the depth-averaged, leading-order momentum equations read

$$\begin{aligned} &\frac{\partial}{\partial t}\left(J_{\text{b}} h^{\text{s}} v^{\text{s}}_x\right) + \frac{\partial}{\partial \xi}\Big(J_{\text{b}} h^{\text{s}} v^{\text{s}}_x v^{\text{s}}_{\xi} + \epsilon J_{\text{b}} h \Omega^{-1}_{11} \overline{N}^{\text{s}}\Big) + \frac{\partial}{\partial \eta}\Big(J_{\text{b}} h^{\text{s}} v^{\text{s}}_x v^{\text{s}}_{\eta} + \epsilon J_{\text{b}} h \Omega^{-1}_{21} \overline{N}^{\text{s}}\Big) \\ &\quad = \underbrace{J_{\text{b}} h^{\text{s}} n_x}_{\text{(i)}} - \epsilon \alpha_{\rho} F^{\text{B}}_{1121} + J_{\text{b}} \alpha_{\rho} F^{\text{Rel}}_x - \underbrace{\epsilon J_{\text{b}} h^{\text{s}} n_z \Phi_{1121}}_{\text{(ii)}} - \underbrace{J_{\text{b}} p^{\text{s}}_{\text{b}} \tan \delta_{\text{b}} \frac{v^{\text{s}}_x}{\left\|\mathbf{v}^{\text{s}}\right\|}}_{\text{(iii)}} + \underbrace{\epsilon J_{\text{b}} v^{\text{s}}_{x,\text{b}} \mathcal{E}^{\text{s}}}_{\text{(iv)}} \end{aligned} \tag{8}$$

and

$$\frac{\partial}{\partial t}\left(J_{\mathrm{b}}h^{\mathrm{s}}v^{\mathrm{s}}_{y}\right)+\frac{\partial}{\partial\xi}\Big(J_{\mathrm{b}}h^{\mathrm{s}}v^{\mathrm{s}}_{y}v^{\mathrm{s}}_{\xi}+\epsilon J_{\mathrm{b}}h\Omega^{-1}_{12}\overline{N}^{\mathrm{s}}\Big)+\frac{\partial}{\partial\eta}\Big(J_{\mathrm{b}}h^{\mathrm{s}}v^{\mathrm{s}}_{y}v^{\mathrm{s}}_{\eta}+\epsilon J_{\mathrm{b}}h\Omega^{-1}_{22}\overline{N}^{\mathrm{s}}\Big)$$
$$=\underbrace{J_{\mathrm{b}}h^{\mathrm{s}}n_{y}}_{\text{(i)}}-\epsilon\alpha_{\rho}F^{\mathrm{B}}_{1222}+J_{\mathrm{b}}\alpha_{\rho}F^{\mathrm{Rel}}_{y}-\underbrace{\epsilon J_{\mathrm{b}}h^{\mathrm{s}}n_{z}\Phi_{1222}}_{\text{(ii)}}-\underbrace{J_{\mathrm{b}}p^{\mathrm{s}}_{\mathrm{b}}\tan\delta_{\mathrm{b}}\frac{v^{\mathrm{s}}_{y}}{\left\|\mathbf{v}^{\mathrm{s}}\right\|}}_{\text{(iii)}}+\underbrace{\epsilon J_{\mathrm{b}}v^{\mathrm{s}}_{y,\mathrm{b}}\mathcal{E}^{\mathrm{s}}}_{\text{(iv)}}, \tag{9}$$

of the solid phase, and

$$\frac{\partial}{\partial t}\left(J_{\mathrm{b}}h^{\mathrm{f}}v^{\mathrm{f}}_{x}\right)+\frac{\partial}{\partial\xi}\Big(J_{\mathrm{b}}h^{\mathrm{f}}v^{\mathrm{f}}_{x}v^{\mathrm{f}}_{\xi}+\epsilon J_{\mathrm{b}}h\Omega^{-1}_{11}\overline{N}^{\mathrm{f}}\Big)+\frac{\partial}{\partial\eta}\Big(J_{\mathrm{b}}h^{\mathrm{f}}v^{\mathrm{f}}_{x}v^{\mathrm{f}}_{\eta}+\epsilon J_{\mathrm{b}}h\Omega^{-1}_{21}\overline{N}^{\mathrm{f}}\Big)$$
$$=\underbrace{J_{\mathrm{b}}h^{\mathrm{f}}n_{x}}_{\text{(i)}}+\epsilon F^{\mathrm{B}}_{1121}-J_{\mathrm{b}}F^{\mathrm{Rel}}_{x}+\epsilon F^{\mathrm{Vis}}_{x}\underbrace{-J_{\mathrm{b}}h^{\mathrm{f}}\frac{\vartheta^{\mathrm{f}}_{\mathrm{b}}v^{\mathrm{f}}_{x}}{\epsilon N_{R}}-J_{\mathrm{b}}\Pi^{\mathrm{M}}\frac{n^{2}_{\mathrm{M}}h^{\mathrm{f}}v^{\mathrm{f}}_{x}\left\|\boldsymbol{v}^{\mathrm{f}}\right\|}{h^{\mathrm{f}\,4/3}}}_{\text{(v)}}$$
$$-\underbrace{\epsilon J_{\mathrm{b}}h^{\mathrm{f}}n_{z}\Phi_{1121}}_{\text{(ii)}}+\underbrace{\epsilon J_{\mathrm{b}}v^{\mathrm{f}}_{x,\mathrm{b}}\mathcal{E}^{\mathrm{f}}}_{\text{(iv)}} \tag{10}$$

and

$$\frac{\partial}{\partial t}\left(J_{\mathrm{b}}h^{\mathrm{f}}v^{\mathrm{f}}_{y}\right)+\frac{\partial}{\partial\xi}\left(J_{\mathrm{b}}h^{\mathrm{f}}v^{\mathrm{f}}_{y}v^{\mathrm{f}}_{\xi}+\epsilon J_{\mathrm{b}}h\Omega^{-1}_{12}\overline{N}^{\mathrm{f}}\right)+\frac{\partial}{\partial\eta}\left(J_{\mathrm{b}}h^{\mathrm{f}}v^{\mathrm{f}}_{x}v^{\mathrm{f}}_{\eta}+\epsilon J_{\mathrm{b}}h\Omega^{-1}_{22}\overline{N}^{\mathrm{f}}\right)$$
$$=\underbrace{J_{\mathrm{b}}h^{\mathrm{f}}n_{y}}_{\text{(i)}}+\epsilon F^{\mathrm{B}}_{1222}-J_{\mathrm{b}}F^{\mathrm{Rel}}_{y}+\epsilon F^{\mathrm{Vis}}_{y}\underbrace{-J_{\mathrm{b}}h^{\mathrm{f}}\frac{\vartheta^{\mathrm{f}}_{\mathrm{b}}v^{\mathrm{f}}_{y}}{\epsilon N_{R}}-J_{\mathrm{b}}\Pi^{\mathrm{M}}\frac{n^{2}_{\mathrm{M}}h^{\mathrm{f}}v^{\mathrm{f}}_{y}\left\|\boldsymbol{v}^{\mathrm{f}}\right\|}{h^{\mathrm{f}\,4/3}}}_{\text{(v)}}$$
$$-\underbrace{\epsilon J_{\mathrm{b}}h^{\mathrm{f}}n_{z}\Phi_{1222}}_{\text{(ii)}}+\underbrace{\epsilon J_{\mathrm{b}}v^{\mathrm{f}}_{y,\mathrm{b}}\mathcal{E}^{\mathrm{f}}}_{\text{(iv)}}, \tag{11}$$

for the fluid phase.

In (8) – (11), (v_x, v_y) are the projected components of the tangential velocity (v_ξ, v_η) on the horizontal xy-plane. Since only the tangential velocity is considered (i.e., $v_\zeta \approx 0$), they are related by

$$v_x=\Omega_{11}v_\xi+\Omega_{12}v_\eta\,,\quad v_y=\Omega_{21}v_\xi+\Omega_{22}v_\eta\,,\quad v_z=\Omega_{31}v_\xi+\Omega_{32}v_\eta\,,$$

and

$$v_\xi=\Omega^{-1}_{11}v_x+\Omega^{-1}_{12}v_y+\Omega^{-1}_{13}v_z\,,\qquad v_\eta=\Omega^{-1}_{21}v_x+\Omega^{-1}_{22}v_y+\Omega^{-1}_{23}v_z$$

with Ω_{ij} and Ω^{-1}_{ij} denoting the component of $\boldsymbol{\Omega}_{\mathrm{b}}$ and $\boldsymbol{\Omega}^{-1}_{\mathrm{b}}$, respectively. Notations $\overline{N}^{\mathrm{s}} = n_z(1-\alpha_\rho)h^{\mathrm{s}}/2$ and $\overline{N}^{\mathrm{f}} = n_z h/2$ stand for the depth-averaged pressure of the solid and fluid phase, respectively. The buoyancy forces are denoted by F^{B}_{1121} and F^{B}_{1222} with

$$\begin{aligned}F^{\mathrm{B}}_{1121}&=\phi^{\mathrm{s}}\Big\{\Omega^{-1}_{11}\partial_\xi\left(J_{\mathrm{b}}h\overline{N}^{\mathrm{f}}\right)+\Omega^{-1}_{21}\partial_\eta\left(J_{\mathrm{b}}h\overline{N}^{\mathrm{f}}\right)\Big\},\\ F^{\mathrm{B}}_{1222}&=\phi^{\mathrm{s}}\Big\{\Omega^{-1}_{12}\partial_\xi\left(J_{\mathrm{b}}h\overline{N}^{\mathrm{f}}\right)+\Omega^{-1}_{22}\partial_\eta\left(J_{\mathrm{b}}h\overline{N}^{\mathrm{f}}\right)\Big\},\end{aligned} \tag{12}$$

where we note $\partial_\xi(\cdot) = \partial(\cdot)/\partial\xi$ and $\partial_\eta(\cdot) = \partial(\cdot)/\partial\eta$, and α_ρ (equal to $\rho^{\mathrm{s}}/\rho^{\mathrm{f}}$) stands for the density ratio of flowing body. Notations F^{Rel}_x and F^{Rel}_y represent the drags due to the velocity difference between the two phases,

$$F^{\mathrm{Rel}}_x=c_D\phi^{\mathrm{s}}\phi^{\mathrm{f}}h\left(v^{\mathrm{f}}_x-v^{\mathrm{s}}_x\right)\,,\qquad F^{\mathrm{Rel}}_y=c_D\phi^{\mathrm{s}}\phi^{\mathrm{f}}h\left(v^{\mathrm{f}}_y-v^{\mathrm{s}}_y\right) \tag{13}$$

with c_D the drag (between the constituents) coefficient. For the fluid phase,

$$
\begin{aligned}
F_x^{\mathrm{Vis}} &= \frac{\phi^{\mathrm{f}}}{N_R}\Big\{2\partial_\xi\Big[J_{\mathrm{b}}h\left(\Omega_{11}^{-1}\partial_\xi v_\xi^{\mathrm{f}}+\Omega_{21}^{-1}\partial_\eta v_\xi^{\mathrm{f}}\right)\Big] \\
&\qquad +\partial_\eta\Big[J_{\mathrm{b}}h\big(\Omega_{12}^{-1}\partial_\xi v_\xi^{\mathrm{f}}+\Omega_{22}^{-1}\partial_\eta v_\xi^{\mathrm{f}}+\Omega_{11}^{-1}\partial_\xi v_\eta^{\mathrm{f}}+\Omega_{21}^{-1}\partial_\eta v_\eta^{\mathrm{f}}\big)\Big]\Big\} \\
F_y^{\mathrm{Vis}} &= \frac{\phi^{\mathrm{f}}}{N_R}\Big\{\partial_\xi\Big[J_{\mathrm{b}}h\left(\Omega_{12}^{-1}\partial_\xi v_\xi^{\mathrm{f}}+\Omega_{22}^{-1}\partial_\eta v_\xi^{\mathrm{f}}+\Omega_{11}^{-1}\partial_\xi v_\eta^{\mathrm{f}}+\Omega_{21}^{-1}\partial_\eta v_\eta^{\mathrm{f}}\right)\Big] \\
&\qquad +2\partial_\eta\Big[J_{\mathrm{b}}h\left(\Omega_{12}^{-1}\partial_\xi v_\eta^{\mathrm{f}}+\Omega_{22}^{-1}\partial_\eta v_\eta^{\mathrm{f}}\right)\Big]\Big\}
\end{aligned}
\tag{14}
$$

account for the viscous effects, where $N_R = \rho^{\mathrm{f}}\mathcal{H}\sqrt{g\mathcal{L}}/\mu^{\mathrm{f}}$ with μ^{f} the fluid viscosity and g the gravitational acceleration (cf. [3]).

On the right-hand side of (8) – (11), terms (i) are the components of the normal pressure at the bottom, which are caused by the reaction force of gravity; terms (ii) represent the effects caused by the sub-topography on the smoothed reference surface; terms (iii) indicate the basal drags with δ_{b} being the angle of basal friction of the solid phase; terms (iv) stand for the momentum loss due to erosion/deposition; and terms (v) denote the basal drags for the fluid phase. Terms (ii) are introduced to account for the effects caused by the "sub-topography", where

$$
\Phi_{1121} = \Omega_{11}^{-1}\partial_\xi\zeta_{\mathrm{b}} + \Omega_{21}^{-1}\partial_\eta\zeta_{\mathrm{b}} \qquad \text{and} \qquad \Phi_{1222} = \Omega_{12}^{-1}\partial_\xi\zeta_{\mathrm{b}} + \Omega_{22}^{-1}\partial_\eta\zeta_{\mathrm{b}}\,. \tag{15}
$$

The aspect ratio ϵ in terms (ii) indicates that the topography gradients (with respect to the smoothed reference surface), $\partial_\xi\zeta_{\mathrm{b}}$ and $\partial_\eta\zeta_{\mathrm{b}}$, should be small (i.e., shallow topography). In terms (iii) and (v), $\|\mathbf{v}\| = \left[(v_x)^2+(v_y)^2+(v_z)^2\right]^{1/2}$ represents the speed of the solid/fluid constituent. In terms (iii) for the solid phase, $p_{\mathrm{b}}^{\mathrm{s}} = h^{\mathrm{s}}n_z\left[1-\epsilon^\chi a_{\mathrm{curv}}^{\mathrm{s}} - \alpha_\rho(1-\epsilon^\chi a_{\mathrm{curv}}^{\mathrm{f}})\right]$ means the solid pressure at the basal surface, where the centripetal accelerations of the two constituents,

$$
\begin{aligned}
a_{\mathrm{curv}}^{\mathrm{s}} &= v_x^{\mathrm{s}}(\partial_\xi n_x)v_\xi^{\mathrm{s}} + v_y^{\mathrm{s}}(\partial_\xi n_y)v_\xi^{\mathrm{s}} + v_z^{\mathrm{s}}(\partial_\xi n_z)v_\xi^{\mathrm{s}} + v_x^{\mathrm{s}}(\partial_\eta n_x)v_\eta^{\mathrm{s}} + v_y^{\mathrm{s}}(\partial_\eta n_y)v_\eta^{\mathrm{s}} + v_z^{\mathrm{s}}(\partial_\eta n_z)v_\eta^{\mathrm{s}} \\
a_{\mathrm{curv}}^{\mathrm{f}} &= v_x^{\mathrm{f}}(\partial_\xi n_x)v_\xi^{\mathrm{f}} + v_y^{\mathrm{f}}(\partial_\xi n_y)v_\xi^{\mathrm{f}} + v_z^{\mathrm{f}}(\partial_\xi n_z)v_\xi^{\mathrm{f}} + v_x^{\mathrm{f}}(\partial_\eta n_x)v_\eta^{\mathrm{f}} + v_y^{\mathrm{f}}(\partial_\eta n_y)v_\eta^{\mathrm{f}} + v_z^{\mathrm{f}}(\partial_\eta n_z)v_\eta^{\mathrm{f}}\,,
\end{aligned}
$$

are considered (cf. [6, 1, 3]). The terms (v) consist of two parts, the first one refers to the Navier drag as employed in Tai et al.,[3], and the second part stands for the Manning drag [7], where n_{M} stands for the Manning coefficient, and $\Pi^{\mathrm{M}} = \mathcal{H}^{4/3}/(g\mathcal{L})$ is a factor for the consistency of dimension.

It is noted that the reference surface becomes a flat plane after smoothing the topography for infinite times. Consequently, the model equations are transformed into Cartesian coordinates, as elaborated in [5]. However, a highly rugged topography results in large topography gradients, where the small aspect ratio ϵ in terms (ii) indicates the necessity for a gradual variation of the topographic surface. The present approach provides a smoothed reference surface for constructing the coordinate system, while maintaining the gentle topography gradients.

2.3 Erosion and deposition rates

In Wong et al., [5], the erosion-deposition (volume) rate is suggested to be the sum of the erosion and deposition rates, i.e.,

$$
\mathcal{E}^{\mathrm{s}} = E^{\mathrm{s}} - D^{\mathrm{s}}\,, \tag{16}
$$

where they are determined by

$$
E^{\mathrm{s}} = \max\Big(0.0,\ \alpha_E\sqrt{h}\Big(\tilde{\Psi}-\tilde{\Psi}_{\mathrm{th}}\Big)\phi_{\mathrm{b}}^{\mathrm{s}}\Big) \qquad \text{and} \qquad D^{\mathrm{s}} = \max\Big(0.0,\ \alpha_D\,\omega\Big(\tilde{\Sigma}_{\mathrm{b}}-\tilde{\Sigma}_{\mathrm{th}}\Big)\Big) \tag{17}
$$

with α_E and α_D the erosion and deposition coefficients, respectively. In $(17)_1$, $\tilde{\Psi}$ is related to the Shields parameter suggested in [8],

$$
\tilde{\Psi} = \frac{\tau_{\mathrm{b}}^{\mathrm{total}}}{(1-\alpha_\rho)\,d} \qquad \text{with} \qquad \tau_{\mathrm{b}}^{\mathrm{total}} = p_{\mathrm{b}}^{\mathrm{s}}\tan\delta_{\mathrm{b}} + \alpha_\rho\left\{\frac{\vartheta_{\mathrm{b}}^{\mathrm{f}}h^{\mathrm{f}}\left\|\boldsymbol{v}^{\mathrm{f}}\right\|}{\epsilon N_R} + \Pi^{\mathrm{M}}\frac{n_{\mathrm{M}}^2h^{\mathrm{f}}\left\|\boldsymbol{v}^{\mathrm{f}}\right\|^2}{{h^{\mathrm{f}}}^{4/3}}\right\}. \tag{18}
$$

Table 1: Parameter values for simulating the debris flow in testing example and Hsiaolin event (HS)

	Testing Example	Hsiaolin event (HS)	Description
$\epsilon = \mathcal{H}/\mathcal{L}$	0.1 m/0.1 m	10 m/10 m	aspect ratio
$\alpha_\rho = \rho^{\rm f}/\rho^{\rm s}$	1.42/2.60	1.42/2.60	density ratio
x	∈[0, 90] m	∈[0, 3,700] m	computational domain
y	∈[-20, 20] m	∈[0, 2,210] m	computational domain
$\Delta x = \Delta y$	0.2 m	10 m	mesh size
$\delta_{\rm b}$	14.2°	14.2°	angle of basal friction (solid phase)
$\vartheta^{\rm f}_{\rm b}$	5.0	5.0	Navier fluid friction coefficient
c_D	6.0	6.0	drag coefficient
$\mu^{\rm f}$	0.5245 Pa · s	0.5245 Pa · s	viscosity of interstitial fluid
N_R	268	268	viscous number
d	n.a.	5 (0.5 m)	sediment median diameter
$\tilde{\Psi}_{\rm th}$	n.a.	0.054	threshold for Shields parameter
$\tilde{\rm v}_{\rm lim}$	n.a.	1.6	critical speed for deposit
ω	n.a.	2.1777	sediment settling speed (dimensionless)
$\tilde{\Sigma}_{\rm th}$	n.a.	0.016	threshold for deposit
$\phi^{\rm f}_{\rm b}$	n.a.	0.38	porosity of bottom
α_E	0.0	0.00008	erosion coefficient
$\alpha_{\rm D}$	0.0	0.04	deposition coefficient
$n_{\rm M}$	0.03	0.03	Manning's coefficient
$\Pi^{\rm M}$	0.04736	0.04736	factor for Manning coefficient
CFL	0.1	0.1	CFL number

Here, d represents the sediment (median) diameter, and $\tau_{\rm b}^{\rm total}$ denotes the resultant basal friction, which is the sum of the basal drags caused by both constituents. As indicated in $(17)_1$, no erosion occurs when $\tilde{\Psi} \leq \tilde{\Psi}_{\rm th}$. The threshold value $\tilde{\Psi}_{\rm th}$ depends on the mean diameter of the sediments as listed in [9]. In $(17)_2$, ω means the sediment settling speed and $\tilde{\Sigma}_{\rm b}$ includes the dependences of the flow speed and the mean sediment diameter,

$$\omega = \left[\left(\frac{13.95}{N_R\, d}\right)^2 + 1.09\epsilon d\left(\frac{1-\alpha_\rho}{\alpha_\rho}\right)\right]^{1/2} - \frac{13.95}{N_R\, d} \qquad \text{and} \qquad \tilde{\Sigma}_{\rm b} = \left(\tilde{\rm v}_{\rm lim} - \frac{\|\boldsymbol{v}^{\rm s}\|}{\sqrt{d}}\right)\phi^{\rm s}\,. \tag{19}$$

Eq. $(19)_1$ is an empirical formula suggested by [10]. Notation $\tilde{\rm v}_{\rm lim}$ in Eq. $(19)_2$ is a critical speed, above which no deposit takes place, and its value can be determined by means of the Hjulström-Sundborg diagram (see [11, 12]), and $\tilde{\Sigma}_{\rm th} = 0.01\,\tilde{\rm v}_{\rm lim}$ is set in the present study.

3 Numerical examples

The equation system, (6) – (11) and (16) – (17), is implemented based on a CUDA-GPU-accelerated simulation tool, MoSES_2PDF developed by [13], in which the anti-diffusive, nonoscillatory central scheme proposed by [14, 15] is employed. To achieve high accuracy in time and space, the two-step modified Euler (second-order RK) method is adopted, and the Minmod TVD slope limiter is utilized in cell reconstruction. For time marching, the time interval Δt is calculated with a constant Courant-Friedrichs-Lewy number (CFL= 0.1) at each time step. We refer the readers to [3, 13] for details.

The model equations are derived and given in dimensionless form. We choose $\mathcal{H} = \mathcal{L} = 0.1\,$m for the transformation between the dimensionless variables and dimensional ones, so that one unit of dimensionless length is equal to 0.1 m and 0.101 s for one dimensionless time unit. The dimensionless parameters used in the computation and their associated physical quantities are summarized and listed in Table 1, wherein the following relations have been utilized,

$$\begin{aligned}
\Big(x,\, y,\, z,\, z_{\rm b}, \xi,\, \eta,\, \zeta,\, \zeta_{\rm b},\, d\Big)_{\rm dim} &= \mathcal{L}\Big(x,\, y,\, z,\, z_{\rm b}, \xi,\, \eta,\, \epsilon\,\zeta,\, \epsilon\,\zeta_{\rm b},\, \epsilon\, d\Big)_{\rm non}\,, \\
\Big(v_x, v_y, v_z, v_\xi, v_\eta, \omega, t\Big)_{\rm dim} &= \sqrt{g\mathcal{L}}\Big(v_x, v_y, v_z, v_\xi, v_\eta, \omega, t/g\Big)_{\rm non}\,, \\
\Big(\alpha_E,\, \alpha_D,\, \tilde{\Psi}_{\rm th},\, \tilde{\Sigma}_{\rm b},\, \tilde{\Sigma}_{\rm th}\Big)_{\rm dim} &= \Big(\epsilon^{1/2}\alpha_E,\, \epsilon^{3/2}\alpha_D,\, \tilde{\Psi}_{\rm th},\, \epsilon^{-1/2}\tilde{\Sigma}_{\rm b},\, \epsilon^{-1/2}\tilde{\Sigma}_{\rm th}\Big)_{\rm non}\,.
\end{aligned} \tag{20}$$

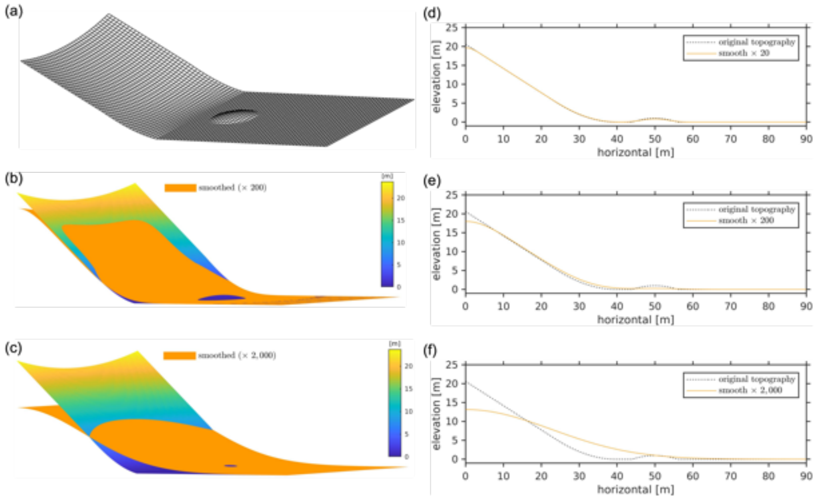

Figure 3: Chute geometry, smoothed basal surfaces and sectional views after various smoothing processes.

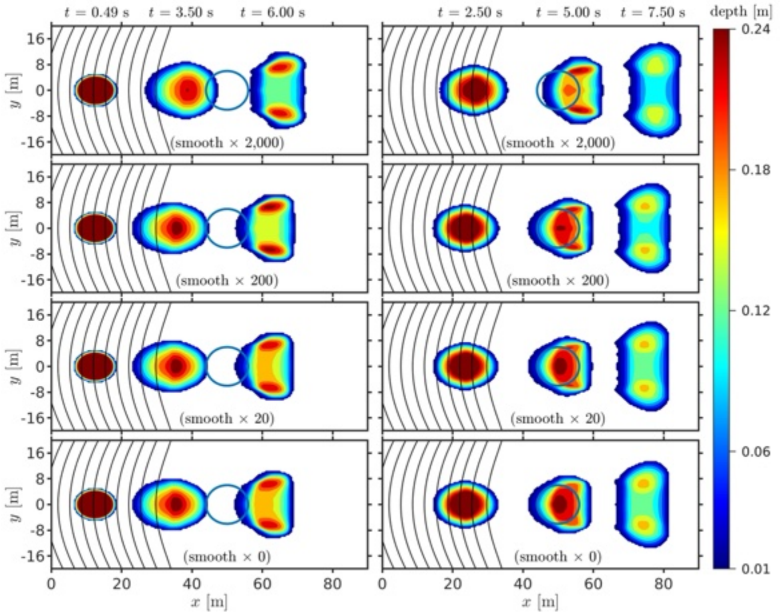

Figure 4: Topography contours and results computed with various smoothing reference surfaces at time levels t = 0.49, 2.5, 3.50, 6.00 and 7.50 s, where the smoothing number 0, 20, 200 and 2,000 are considered. The outline of the bump obstacle on the horizontal plane is marked by the solid cyan line.

3.1 Idealized testing example

We consider a finite mass of grain-fluid mixture released from the state of rest, flowing down an inclined curved chute and merging into a horizontal deposition zone. The chute consists of three sections: the inclined section, the transition zone, and the horizontal plane. As shown in Fig. 3a, the inclined section is curved with a parabolic concave profile in the cross-slope direction, and a bump exits on the horizontal plane as an additional obstacle. The chute covers $x \in [0, 90]$ m and $y \in [-20, 20]$ m, of which the inclined part lies in the range for $x \leq 24$ m, and the horizontal flat plane ranges from $x \geq 40$ m. In the transition zone, the inclination angle linearly decreases from $\varphi_0 = 40°$ to zero. In the cross-slope y-direction, the inclined section, $(x \leq 24)$, is curved with an additional elevation $z_{\text{add}} = y^2/100 \cos\varphi(x)$ on the inclined flat plane, where the magnitude of z_{add} linearly decrease to zero when merging into the horizontal plane. Besides, a parabolic bump with a height of 1 m and a radius of 6.0 m centered at (50.0, 0.0) is added as obstacle on the horizontal plane. Figure 3bc show the smoothed reference surface (in orange color) with 200 and 2,000 times of smoothing process by the filter given in (3). Figure 3ef are the corresponding sectional views of the original (black dashed line) and smoothed (orange solid line) basal surface along $y = 0$, and Fig. 3d depicts the sectional view for the case of 20 smoothing processes.

The initial mass comprises a parabolic shell, $h(x, y, t)$, with the center of the shell at $(x, y) = (12.0, 0.0)$. The computational domain covers $x \in [0, 90]$ and $y \in [-20, 20]$ with totally 181×81 meshes. Figure 4 illustrates the computed results with respect to the coordinate surface constructed by 0, 20, 200 and $2,000$ smoothing processes at time levels $t = 0.49$, 2.5, 3.50, 6.00 and 7.50 s, where the bump obstacle on the horizontal plane is outlined by the solid cyan line. Neither erosion nor deposition is considered in this campaign. The results well demonstrate the impacts of the “sub-topography” over the smoothed reference surface on the flow behavior. The longest traveling distance and the widest extension in cross-slope direction are found in the computation with the coordinate surface after a smoothing process of $2,000$ times. In terms of the distribution of flow thickness, no significant impact can be found when the number of smoothing process is up to 20 times. Henceforth, the smoothing process of 20 times is adopted in the application of a large-scale event, to investigate the impacts of the smoothing process on both the flow paths and erosion/deposition.

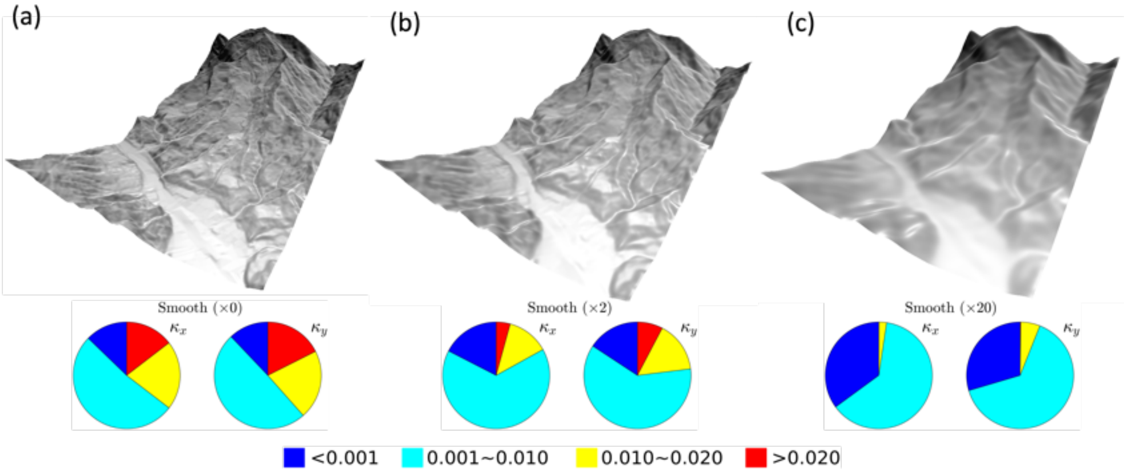

Figure 5: The smoothed reference surfaces. (a) Without smoothing process. (b) With process of smoothing 2 times. (c) With process of smoothing 20 times. The 3D imagines are given by the ANSI-Platform, and the lower pie charts illustrate the corresponding curvatures of the reference surfaces in x- and y-directions (cf. Table 2).

Table 2: Percentage of curvature radii R_{curv} after various smoothing processes (cf. Fig. 5)

	without smoothing		smoothed ×2		smoothed ×20	
	$\lvert\kappa_x\rvert$	$\lvert\kappa_y\rvert$	$\lvert\kappa_x\rvert$	$\lvert\kappa_y\rvert$	$\lvert\kappa_x\rvert$	$\lvert\kappa_y\rvert$
$R_{\text{curv}} \geq 1,000\,\text{m}$	12.8%	12.1%	17.4%	15.7%	35.1%	29.6%
$1,000 > R_{\text{curv}} \geq 100\,\text{m}$	51.8%	49.5%	65.6%	61.2%	62.6%	64.4%
$100 > R_{\text{curv}} \geq 50\,\text{m}$	20.9%	20.9%	12.7%	15.4%	2.3%	5.8%
$R_{\text{curv}} < 50\,\text{m}$	14.6%	17.6%	4.3%	7.7%	0.03%	0.19%

3.2 Application to large-scale event

The proposed approach with smoothed-reference surface is applied to simulating the flow behavior in a historical event, the 2009 Hsiaolin (HS) event, which took place during the Typhoon Morakot in 2009 in the mountain area in southern Taiwan. In this event there are ca. 2.4 ± 2 Mm^3 of displaced material, and the traveling distance reaches up to 2.8 km. In the simulation, the used DEM and initial released masses are identical to the ones used in [12], and the DEM is with a resolution of 10 m. Three cases are considered, that the reference surfaces are smoothed by 0, 2, and 20 times, and they are indexed by “HS-F00”, “HS-F02”, and “HS-F20”, respectively. Figure 5 shows the 3D views of the reference surface after

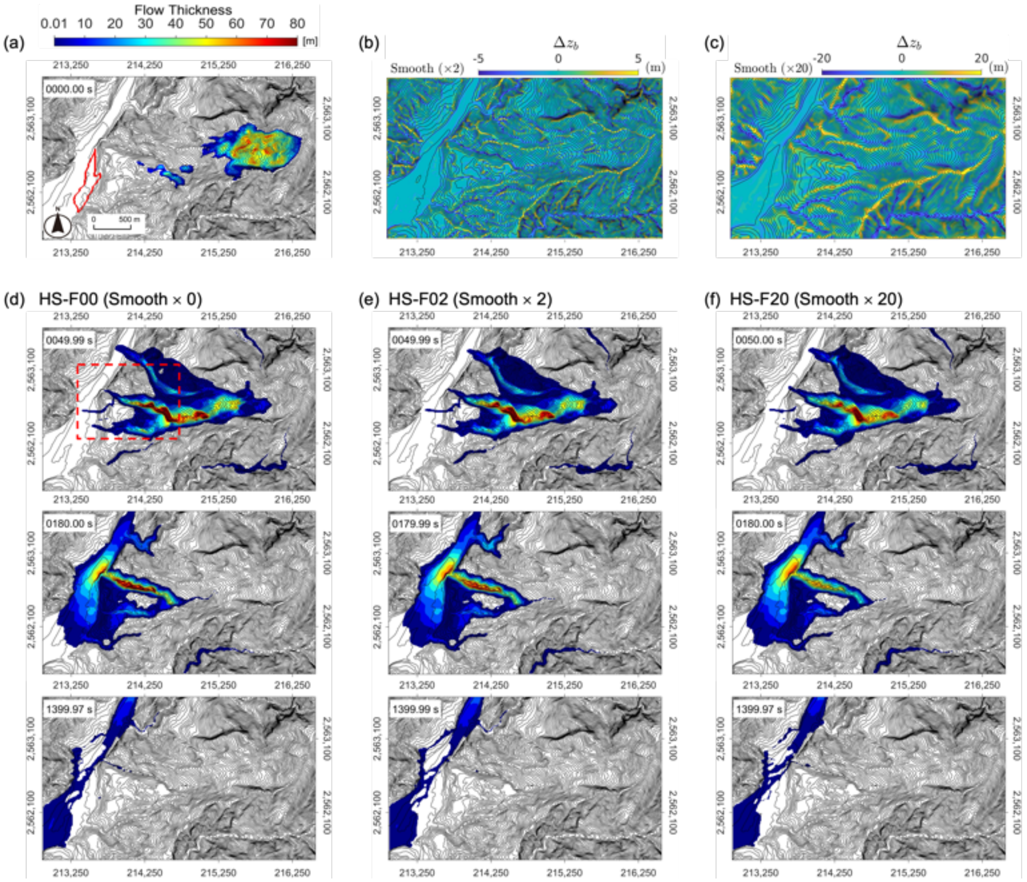

Figure 6: (a) Contour plots of the topography and the released mass in HS case, where the red-line marked area indicate the location of Hsiaolin village. (b) & (c) Contour plots of the reference surface with smoothing process of 2 and 20 times, respectively, where the corresponding Δz_{b} are shown by color scales. (d) – (f) Flow thickness computed with reference surface with smoothing process of 0, 2 and 20 times, respectively.

smoothing process of 0, 2, and 20 times, respectively, while the bottom panels present the associated curvatures in x- and y-directions as percentages. The percentage of high curvatures ($\kappa_{x,\,y} > 0.02$, equivalent to a curvature radius less than 50 m) significantly reduces from about 17.6% to 7.7% and 0.2% after smoothing of 2 and 20 times, respectively. Figure 6a illustrates the contour plots of the topography and the released mass in HS case, where the red-line-marked area indicate the location of Hsiaolin village. The contour plots of the reference surface after smoothing process of 2 and 20 times, respectively, along with the corresponding elevation difference Δz_{b} (shown by color scales), are depicted in Fig. 6bc. In the panel (b) of Fig. 6, the elevation difference Δz_{b} ranges from -30.1 to 17.1 m, just after two times of smoothing process. With smoothing process of 20 times, Δz_{b} increases to be in the range of $[-45.5, 41.6]$ m. In both panels (b) and (c), the extreme values indicate either the peak locations (light yellow) or valley areas (dark blue). It is noted that the maximum terrain elevation difference is more than $1,010$ m.

Panels in columns (d), (e) and (f) of Fig. 6 show the distributions of flow thickness at time levels 50, 180 and $1,400$ s, where the results are computed with respect to the smoothed reference surfaces by 0, 2, and 20 times, respectively. These results are in good agreement with previous studies, e.g., the single-phase model in [16, 17], the two-phase approach [3], the simplex multi-phase model [4], and the two-phase model over erodible bed [5]. Although there are approximately three major flow lines, most of the material is aggregated in the middle flow branch (main stream as marked in the red dashed square in Fig. 6d). The results indicate that these reference surfaces do not have significant impacts on the distributions of the flow body, even the erosion and deposition are taken into account. Together with the evolutions of the volume of moving mass (see Fig. 7), only tiny discrepancy of the mass amount in mobility can be found. As shown in Fig. 7, the mass volume reaches the maximal magnitude at about 98 s, reduces to the initial amount at ca. 180 s, while most of the material has deposited at $1,400$ s.

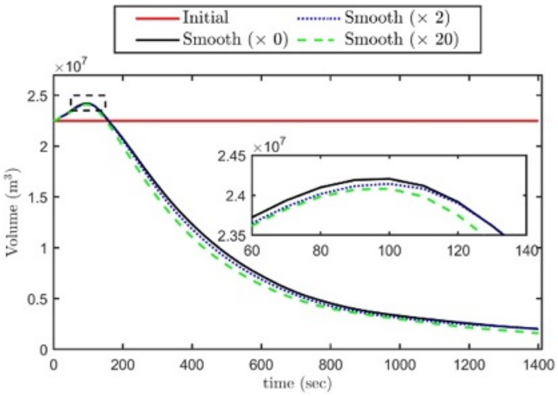

Figure 7: Evolution of the total volume of the moving mass, with the inset showing a local view around $t = 98$ s.

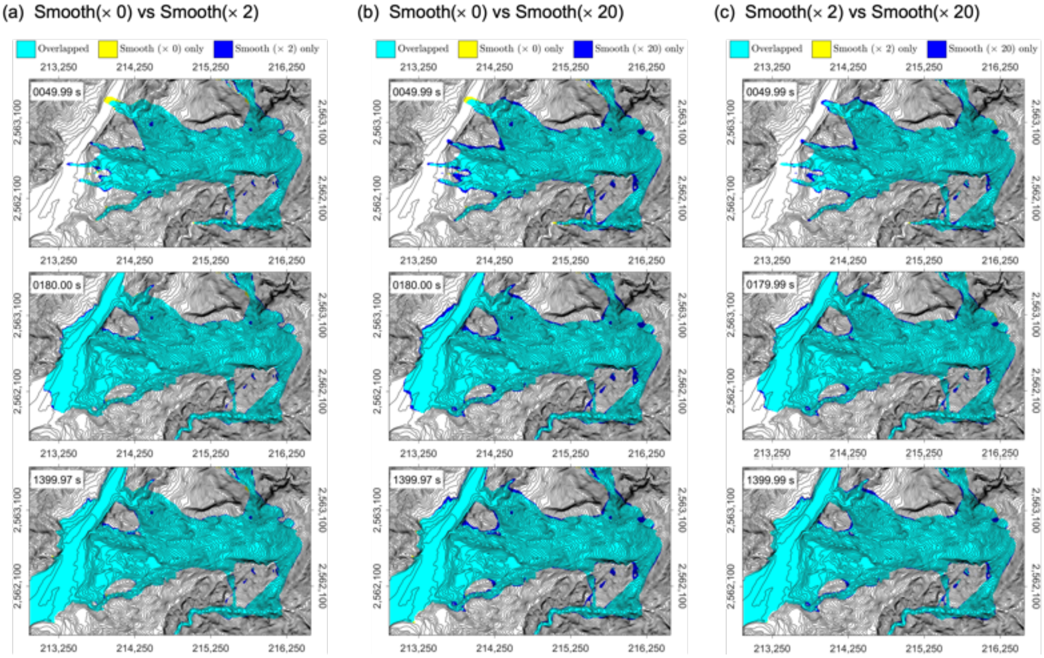

Figure 8: Discrepancies of flow paths computed between different reference surfaces. (a) Smooth (×0) vs Smooth (×2). (b) Smooth (×0) vs Smooth (×20). (b) Smooth (×2) vs Smooth (×20).

Consequently, as shown in Fig. 8, no significant discrepancy among the flow paths can be identified. It is noted that in both Figs. 7 and 8, the results of flow thickness less than 0.01 cm are filtered. So, the discrepancies in the flow paths are tiny. Nonetheless, Fig. 7 reveals the tendency that the smoothed reference surface may results in a slightly less volume of flow body during the movement, i.e. slightly weaken the erosion and slightly enhance the deposition.

Some differences can be identified when one examines the depths of the erosion scar or deposition heap. Figure 9 illustrates the erosion and deposition depths computed with the three reference surfaces. At the first glance, either the erosion scars or the deposition heaps are rather similar. Significant discrepancies are found in the Anonymous Creek Valley locating northern from the Hsiaolin village, the square area marked by red-dashed line. The local views are depicted in Fig. 10. At $t = 50$ s, the material of the main stream flows through the Anonymous Creek Valley with high speed, so that the erosion process dominates at the bottom. The patterns of erosion scar among the three cases are similar. Higher erosion depth is identified in the case HS-F00 at $t = 180$ s, where no smoothing process is used for the reference surface. At this stage, one can find that the smoothing process weakens the erosion. In the period $t \in [180, 1400]$ s, the deposition process dominates, and the deposition heap develops from the river bed into the valley. In both cases of HS-F00 and HS-F02, significant erosion scar is found on the southern slope of the valley and deposition heap develops on the northern slope. One can find that, in the HS-F20 case, the depth

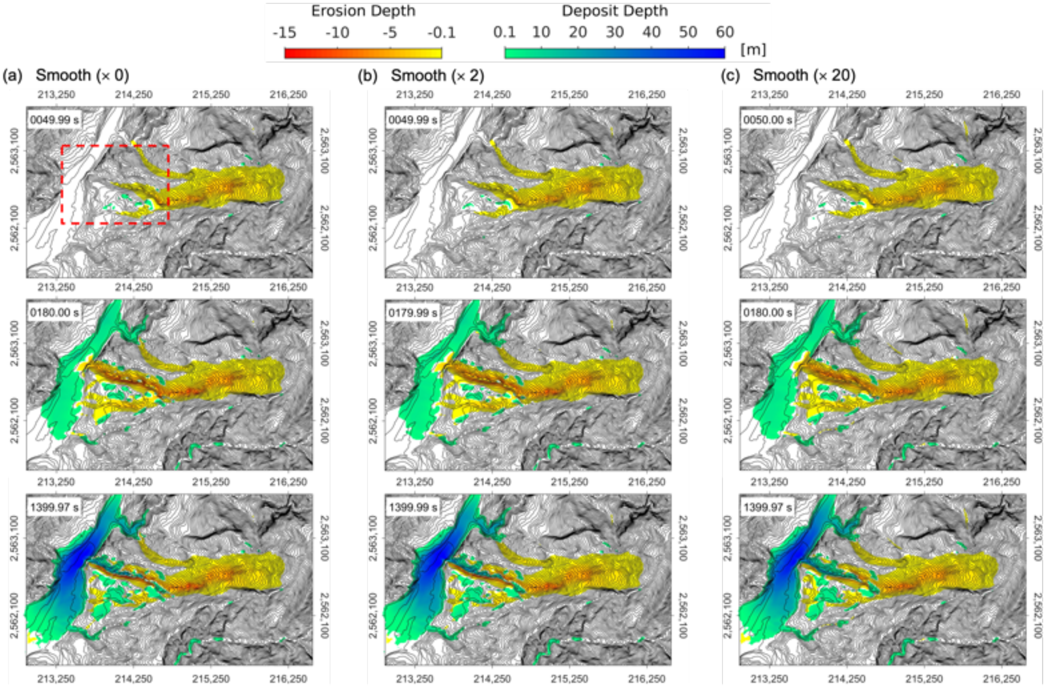

Figure 9: Depths of erosion and heights of the deposition heap. (a) Without smoothing process (HS-F00). (b) With smoothing process of 2 times (HS-F02). (c) With smoothing process of 20 times (HS-F20).

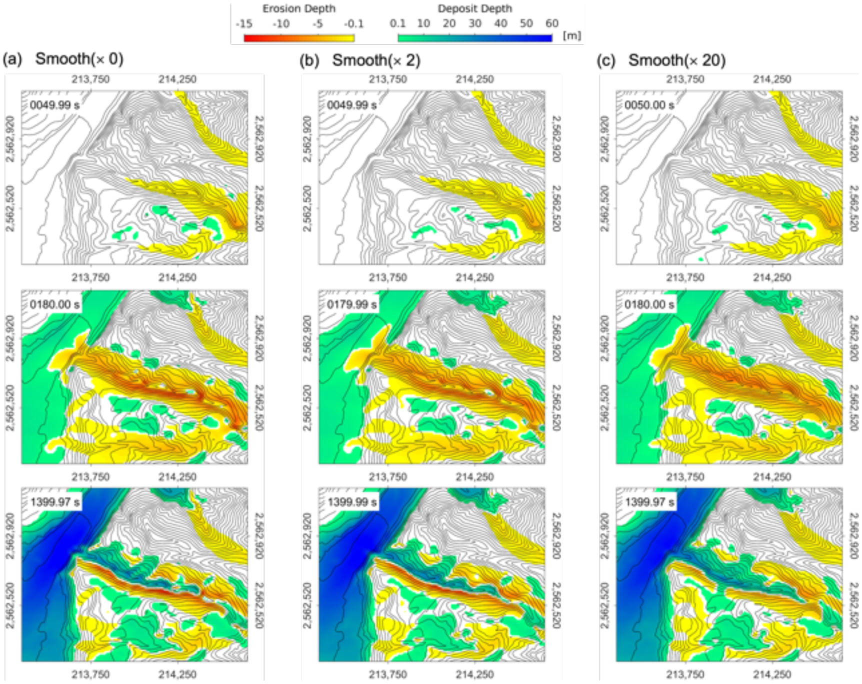

Figure 10: Local views of the red dashed line marked area in Fig. 9. (a) Without smoothing process (HS-F00). (b) With smoothing process of 2 times (HS-F02). (c) With smoothing process of 20 times (HS-F20).

of erosion on the souther slope is more gentle in comparison with the ones in HS-F00 or HS-F02, but the height of the deposition heap on the northern slope covers a slightly larger area. That is, the smoothing process may slightly weaken the erosion and slightly enhance the deposition. It is suspected that the sub-topography ζ_b on the smoothed reference surface is computed based on mass conservation with respect to the elevation difference Δz_b, yielding a more gentle magnitude for ζ_b (cf. (4)) as well as for the depths of erosion/deposition heap. The results in Figs. 6 to 10 reveal that no significant discrepancy for the flow paths can be identified among the three cases, but the erosion/deposition behaviors may be distinct. Here we would like to emphasize that the erodible bottom is assumed to be homogenous and no local geological conditions, such as the bedrock or colluvium, is considered in the computation. So, the discussion focuses on the impacts of the smoothed reference surfaces on the flow paths and the erosion-deposion heaps.

4 Concluding remarks

The key advantage of depth-integration process for modeling gravity-driven flows on non-trivial topographic surfaces is the reduction of computational complexity, where a two-dimensional model equations are needed for describing the flows over a three-dimensional topography. In the depth-integration approach, the directions of the depth-averaged velocity are parallel to the coordinate axes, so that the employed coordinate system plays a crucial role in terms of accuracy. In the present study, we propose a general approach, which integrates the terrain-following coordinate and the conventional (vertically-horizontally-oriented) Cartesian coordinate systems for modeling gravity-driven shallow flows over rugged topographies. The employment of the depth-integration process (for reducing the complexity of computation) results in the depth-averaged velocities parallel to the coordinate directions. This characteristic induces high deviation in the direction of the averaged velocity, when the topography added to the coordinate axis/plane is significant, because the flow follows on the basal surface. The terrain-following coordinate system can mitigate this shortcoming, but it is generally limited by the employment of a shallow curvature of the topographic surface. In the present approach, the terrain-fitted coordinate axes are assigned to coincide with a smoothed basal surface, on which a highly rugged landform (called "sub-topography") is added for reproducing the pre-smoothed topography. In comparison with the conventional Cartesian coordinate, this approach reduces the deviation of the flow velocity direction, and the constraint of shallow curvature is fulfilled without losing the precision of the landform. Furthermore, after performing Gaussian filtering for infinite times, the coordinate axes tend to be straight and comparable to the Cartesian ones. In other words, the proposed approach unifies the terrain-fitted coordinate system and the Cartesian coordinate one.

In the numerical example of idealized chute, no significant discrepancy is found between the results computed with the pre-smoothed surface and with smoothing process up to 20 times (see Fig. 4), where no erosion-deposition is taken into account. In the back-calculation of historical event (2009 Hsaiolin landslide event in Taiwan) for examining the key features of the present approach, the erosion-deposition process is taken into account. As listed in Table 2, twice performances of the smoothing process can reduce the area of high curvature (curvature radius < 50 m) by more than 55%, and more than 99% in case of smoothing for 20 times. The results reveal that, with smoothing process up to 20 times, the smoothed reference surfaces do not have significant influences on the flow paths. However, the employment of the smoothing process may slightly weaken the erosion process and slightly enhance deposition in the Anonymous Creek Valley in the Hsiaolin cases, although the difference of the maximum total volume for the moving mass is less than 0.5%. With the significant reduction of large curvature areas and the low deviation of the depth-averaged velocity from the tangential directions of the basal surface, high potential for the present approach in engineering applications can be expected.

Acknowledgments

The financial support of the National Science and Technology Council, Taiwan (NSTC 112-2221-E-006 -051-MY3) is sincerely acknowledged.

References

[1] Yih-Chin Tai, Chih-Yu Kuo, and Wai-How Hui. An alternative depth-integrated formulation for granular avalanches over temporally varying topography with small curvature. *Geophysical & Astrophysical Fluid Dynamics*, 106(6):596–629, 2012.

[2] Ioana Luca, Yih-Chin Tai, Chih-Yu Kuo, et al. *Shallow geophysical mass flows down arbitrary topography.* Springer, 2016.

[3] Yih-Chin Tai, Julian Heß, and Yongqi Wang. Modeling two-phase debris flows with grain-fluid separation over rugged topography: Application to the 2009 Hsiaolin event, Taiwan. *Journal of Geophysical Research: Earth Surface*, 124(2):305–333, 2019.

[4] Yih-Chin Tai, Hock-Kiet Wong, and Ching-Yuan Ma. A simplex multi-phase approach for modelling debris flows in smoothed-terrain-following coordinate system. In *E3S Web of Conferences*, volume 415, page 02022. EDP Sciences, 2023.

[5] Hock-Kiet Wong, Yih-Chin Tai, Haruka Tsunetaka, and Norifumi Hotta. Two-phase approach to modeling the grain-fluid flows with deposition and entrainment over rugged topography. *Advances in Water Resources*, page 104691, 2024.

[6] Xiannan Meng and Yongqi Wang. Modelling and numerical simulation of two-phase debris flows. *Acta Geotechnica*, 11(5):1027–1045, 2016.

[7] Shuangcai Li and Christopher J Duffy. Fully coupled approach to modeling shallow water flow, sediment transport, and bed evolution in rivers. *Water Resources Research*, 47(3), 2011.

[8] Albert Shields. *Application of similarity principles and turbulence research to bed-load movement.* Pasadena, CA: California Institute of Technology, 1936.

[9] Charles Berenbrock and Andrew W Tranmer. *Simulation of flow, sediment transport, and sediment mobility of the lower Coeur d'Alene River, Idaho*, volume 5093. US Geological Survey Reston, VA, 2008.

[10] RJ Zhang. *Sediment dynamics in rivers.* Hydraulic and Water Power Press of China, Beijing, 1989.

[11] Filip Hjulström. *Studies of the morphological activity of rivers as illustrated by the River Fyris.* PhD thesis, The Geological institution of the University of Upsala, 1935.

[12] Steven Earle. *Physical geology.* BCcampus, 2015.

[13] Chi-Jyun Ko, Po-Chih Chen, Hock-Kiet Wong, and Yih-Chin Tai. MoSES_2PDF: A GIS-compatible GPU-accelerated high-performance simulation tool for grain-fluid shallow flows. *arXiv preprint arXiv:2104.06784*, 2021.

[14] Alexander Kurganov and Eitan Tadmor. New high-resolution central schemes for nonlinear conservation laws and convection–diffusion equations. *Journal of Computational Physics*, 160(1):241–282, 2000.

[15] Alexander Kurganov and Guergana Petrova. A second-order well-balanced positivity preserving central-upwind scheme for the saint-venant system. *Communications in Mathematical Sciences*, 5(1):133–160, 2007.

[16] CY Kuo, Yih-Chin Tai, CC Chen, KJ Chang, AY Siau, JJ Dong, RH Han, T Shimamoto, and CT Lee. The landslide stage of the hsiaolin catastrophe: simulation and validation. *Journal of Geophysical Research: Earth Surface*, 116(F4), 2011.

[17] Yih-Chin Tai, Jeaniffer Vides, Boniface Nkonga, and Chih-Yu Kuo. Multi-mesh-scale approximation of thin geophysical mass flows on complex topographies. *Communications in Computational Physics*, 29(1):148–185, 2021.